Bio-based phase change materials integrated with expanded graphite and Prussian blue for high thermal and photothermal performance in solar energy storage

Wenke Cheng[1], Songping Mo[1,2,*], Kai Fu[1], Yanping Du[3], Zhi Yang[1,2,*], Lisi Jia[1,2], Ying Chen[1,2]

1 School of Materials and Energy, Guangdong University of Technology, Guangzhou 510006, China.

2 Guangdong Provincial Key Laboratory on Functional Soft Condensed Matter, Guangdong University of Technology, Guangzhou 510006, China.

3 School of Engineering, Lancaster University, Lancaster LA1 4YW, UK

Abstract The global shift toward renewable energy has significantly heightened the demand for efficient and sustainable materials for thermal energy storage. Conventional paraffin-based phase change materials (PCMs) are hampered by intrinsic limitations, including poor renewability, susceptibility to leakage, low thermal conductivity and photothermal conversion efficiency. To address these challenges, this study introduces the design and synthesis of novel bio-based eutectic phase change materials (EPCMs) derived from hexadecanol (HD) and various diols. Among them, the hexadecanol–1,12-dodecanediol (HD–DDD) EPCM exhibits the highest latent heat. This EPCM was then integrated with expanded graphite (EG) and Prussian blue (PB) to fabricate a composite PCM for solar thermal energy storage. Through optimization of the EG-to-PB mass ratio, the composite labeled EG14PB10 emerged as the optimal formulation, delivering a latent heat of 180.6 kJ/kg. Its thermal conductivity reached 9.62 W/(m·K), approximately 24.7 times higher than that of pure HD–DDD. Accelerated thermal cycling tests confirmed excellent long-term stability of the composite. Remarkably, the synergistic effect of PB and EG substantially extends solar absorption across the solar spectrum, enabling a photothermal conversion efficiency as high as 93.7%. Owing to its superior thermal performance, high cycling durability, and bio-based composition, the developed EPCM composite stands out as a highly promising candidate for eco-friendly solar thermal energy storage applications.

Keywords: Phase change material, Eutectic, Expanded graphite, Prussian blue, Photothermal

* Corresponding author. *E-mail address*: mosp@ustc.edu (S. Mo), yangzhi@gdut.edu.cn (Z. Yang)

Nomenclature

CPCM	composite phase change material	PB	Prussian blue
DDD	1,12-dodecanediol	PCM	phase change material
DDL	1,10-decanediol	R	molar gas constant
DSC	differential scanning calorimeter	S	illuminated area, m^2
EDS	Energy-dispersive X-ray spectroscopy	SEM	scanning electron microscope
EG	expanded graphite	t	time, s
EPCM	eutectic phase change material	T_f	freezing temperature, ℃
FTIR	Fourier-transform infrared spectrometer	T_m	melting temperature, ℃
H_f	freezing enthalpy, kJ/kg	ΔT_s	supercooling temperature, ℃
H_m	melting enthalpy, kJ/kg	TGA	thermogravimetric analyzer
H_{PCM}	enthalpy of the phase change material, kJ/kg	X	mole fraction
HD	hexadecanol	XRD	X-ray diffractometer
I	light intensity, W/m^2	Greek letters	
LHS	latent heat storage systems	ω	mass fraction
m	mass, kg	Δ	change in parameter
M_{loss}	mass loss percentage	δ	enthalpy percentage deviation
NIR	near-infrared region	η	photothermal conversion efficiency
ODL	1,8-octanediol		

1. Introduction

As the global energy landscape continues to shift from fossil fuels to renewable energy, the share of intermittent renewable sources, such as solar power, is steadily increasing [1-2]. In this context, latent heat storage systems (LHS) based on PCMs have garnered significant attention due to their ability to store and release substantial amounts of heat at nearly constant temperatures. Compared to sensible heat storage, latent heat storage offers several advantages, including higher energy density and near-isothermal energy storage and release and improved energy efficiency, making it particularly suitable for applications in building energy efficiency, industrial waste heat recovery, and solar thermal energy utilization [3-5].

PCMs, as the key functional components of LHS, operate by absorbing or releasing substantial amounts of thermal energy during phase change processes (e.g., solid-liquid phase changes), thereby enabling efficient thermal energy storage and release. PCMs are broadly classified into organic and inorganic types. Among these, organic PCMs, including paraffin waxes, fatty alcohols, and fatty acids, have attracted considerable interest for LHS applications owing to their substantial latent heat, low supercooling tendency, and superior long-term cycling stability. However, paraffin wax-based PCMs are by-products of the petrochemical industry, making them non-renewable and potentially environmentally harmful during production [6]. In contrast, fatty alcohols and fatty acids are bio-based and renewable PCMs derived from biological sources, and are considered more environmentally friendly [7].

Despite the aforementioned advantages of bio-based PCMs, they face the challenge of having a fixed phase change temperature. The use of eutectic mixtures, which are combinations of two or more substances with different melting points to form a mixture with a single melting point, can effectively broaden the operational temperature range of phase change materials [8]. For instance, Ke [9] prepared binary and multi-component EPCMs using various fatty acids, resulting in a series of EPCMs with a temperature range of 14–53 ℃ and latent heat values ranging from approximately 130 to 200 kJ/kg, thus extending the application temperature range of fatty acid-based PCMs. However, some EPCMs obtained in the temperature range of 14–30 ℃ exhibited latent heat values lower than 150 kJ/kg. Rohitash [10] addressed the issue of low latent heat in fatty acid eutectic mixtures by selecting dodecanol to form eutectics with

lauric acid, myristic acid and palmitic acid. The three resulting EPCMs had melting points between 15–20 ℃ and latent heats around 185 kJ/kg. Li [11] developed EPCMs from dodecanol-hexadecanol/octadecanol mixtures for low-temperature solar energy applications. The prepared EPCMs had melting points of 19.6 ℃ and 21.4 ℃, with latent heats of 193.7 kJ/kg and 206.4 kJ/kg, respectively. In addition to fatty alcohol-based EPCMs, saturated diol-based EPCMs have also gained attention owing to their high latent heat. For example, Shen [12] synthesized a stearic acid-1,10-decanediol PCM with a melting temperature of 56.5 ℃ and a latent heat of 247.6 kJ/kg. Fu [13] developed a 1,10-decanediol-paraffin PCM, which exhibited a melting temperature of 63.8 ℃ and a high latent heat of 229.1 kJ/kg. These results demonstrate that fatty alcohol-based and diol-based EPCMs offer clear advantages in latent heat compared to other EPCMs in the same temperature range. These studies underscore the significant latent heat advantages of fatty alcohol-based and diol-based EPCMs within comparable temperature ranges. This superiority is primarily due to the higher phase change enthalpy of fatty alcohols compared to fatty acids and other bio-based PCMs [7]. Moreover, fatty acids tend to be more corrosive than fatty alcohols [14]. Despite these benefits, recent research on bio-based EPCMs has remained heavily concentrated on fatty acid–fatty acid and fatty acid–fatty alcohol systems. For instance, Rimsha [15] and Zhen [16] separately investigated fatty acid-based EPCMs, both of which exhibited relatively low phase change enthalpies (<200 kJ/kg). In contrast, research on alcohol–alcohol EPCMs remain notably limited [8, 11]. Given the inherently high latent heat of pure fatty alcohols, alcohol–alcohol eutectics represent a promising strategy for developing PCMs with enhanced latent heat.

EPCMs can broaden the phase change temperature interval of conventional PCMs. However, the inherent challenges of PCMs, including leakage, low thermal conductivity and limited photothermal conversion efficiency in solar thermal storage applications, remain unresolved. Several strategies have been proposed to tackle these issues, such as the incorporation of thermally conductive fillers [17-18], porous encapsulation [13, 19-20], and micro-nano encapsulation [21-22]. Among these, porous encapsulation has attracted significant attention due to its cost-effectiveness [23]. Various porous materials have been developed for this purpose, including carbon-based porous media, porous ceramics, and metal foams [24].

Notably, expanded graphite stands out due to its abundant porous adsorption sites, extremely high thermal conductivity, low cost, easy availability, and inherent oleophilic properties [25], making it an ideal candidate for encapsulating organic phase change materials. For instance, Chopra [26] encapsulated stearic acid with EG, resulting in a composite phase change material (CPCM) containing up to 90 wt% PCM. Compared with pristine stearic acid, the prepared composite demonstrated a substantially enhanced thermal conductivity, achieving an increase of approximately 345%. This improvement in heat transfer performance contributed to a noticeable reduction in both thermal charging and discharging durations, with the heat storage process shortened by about 11–17% and the heat release period reduced by roughly 17–26%. These results strongly demonstrate potential of EG as a porous medium for enhancing PCM performance.

In solar thermal energy storage applications, photothermal conversion efficiency reflects how effectively a CPCM harnesses solar energy. To enhance this performance, various photothermal agents have been investigated, including carbon-based materials (e.g., carbon nanotubes, graphene oxide) [27-28], metal and metal compound nanoparticles [29-30], and organic polymers (e.g., polyaniline, polydopamine) [1, 19, 31]. However, these materials often suffer from drawbacks such as high production costs, which hinder their widespread adoption in photothermal energy storage systems.

In contrast, Prussian blue, a cost-effective and commercially available inorganic dye, offers several compelling advantages [32]. PB exhibits robust structural stability and strong, tunable light absorption, particularly in the near-infrared (NIR) region. Its molar extinction coefficient in the NIR range rivals that of gold nanoparticles and surpasses that of carbon nanotubes by a significant margin [33]. Leveraging this property, PB can be strategically coupled with materials that absorb strongly in other regions of the solar spectrum. This complementary light-harvesting approach broadens overall solar absorption and substantially enhances the photothermal performance of the resulting composite [34]. The efficacy of this strategy has been demonstrated in various applications. For instance, Cheng [34] synthesized PB in situ on carbonized wood for solar-driven interfacial evaporation, markedly enhancing light absorption and seawater desalination rates. Similarly, Qiu [35] developed a two-

dimensional solar evaporator by integrating PB with polypyrrole, achieving comparable gains in solar-to-thermal conversion efficiency. Maximizing solar-thermal utilization efficiency is critical for enhancing the photothermal performance of composite materials [36]. Recent studies further validate superiority of PB. Achilley et al. [37] demonstrated that PB-containing composites outperform polymeric photothermal materials, while Han et al. [38] highlighted the superior photothermal heating capability of PB.

Although PB is currently well-established in biomedical applications, particularly in cancer photothermal therapy, owing to its excellent biocompatibility and strong NIR absorption [39], its potential in solar thermal energy storage remains comparatively underexplored. Given its favorable optical, economic, and stability properties, PB represents a promising and underutilized candidate for next-generation photothermal energy storage materials.

Building on the above discussion, this work combines hexadecanol, a bio-based PCM with high latent heat and non-corrosive properties, with three diols: 1,8-octanediol (ODL), 1,10-decanediol (DDL), and 1,12-dodecanediol (DDD), to formulate novel EPCMs. These diols are known for their high latent heat and suitability as PCM components [40]. The eutectic compositions were optimized through an integrated approach combining theoretical calculations and experimental validation, leading to the selection of an optimal EPCM. This strategy preserves its high latent heat over other PCMs operating in the same phase change temperature range, underscoring its promise for low-temperature solar thermal energy storage. Moreover, the bio-based composition of these EPCMs aligns with the goals of low-carbon and sustainable development.

Subsequently, EG was employed as both a porous scaffold and a thermally conductive filler to encapsulate the optimized EPCM, yielding a CPCM. A vacuum impregnation method was used to maximize EPCM loading, and PB was added to the composite to further enhance its photothermal conversion efficiency. UV-Vis-NIR spectrophotometric analysis confirmed that PB incorporation dramatically improved the absorbance of CPCM across the solar spectrum. The resulting CPCM was comprehensively characterized using differential scanning calorimetry (DSC), microstructural imaging, chemical compatibility tests, thermal cycling stability assessments, and photothermal performance evaluations. The results demonstrate that

the CPCM features a straightforward fabrication process, environmental benignity, excellent thermal properties, and superior solar absorption, collectively positioning it as a highly promising candidate for solar thermal energy storage applications.

2. Materials and methods

2.1 Materials

Hexadecanol ($CH_3(CH_2)_{14}CH_2OH$, 98%), 1,8-octanediol ($HO(CH_2)_8OH$, 98%), 1,10-decanediol ($HO(CH_2)_{10}OH$, 98%), and 1,12-dodecanediol ($HO(CH_2)_{12}OH$, 98%) were purchased from Shanghai McLean Biochemical Technology Co., Ltd. Expanded graphite (mesh size: 10, fixed carbon content: 99%) was obtained from Nanjing Greifan Carbon Materials Co., Ltd. Prussian blue ($Fe_4[Fe(CN)_6]_3$, biological dye) was sourced from Aladdin Biochemical Technology Co., Ltd.

2.2 Calculation of theoretical eutectic point

The phase change characteristics of the eutectic system comply with the second law of thermodynamics as well as phase equilibrium theory [8]. For alkanes, fatty alcohols, and fatty acids, the saturated liquid-phase boundary of the eutectic system can be described using the simplified Schroeder equation [8, 10-11]. This equation is then employed to construct the binary eutectic phase diagram and identify the optimal eutectic composition.

$$T_{\mathrm{m}} = H_i T_i / (H_i - T_i R In X_i), \ (i = \mathrm{A},\ \mathrm{B}) \tag{1}$$

where T_{m} represents the minimum eutectic temperature (K) of the binary eutectic system, T_i is the melting temperature (K) of the i-th substance, R is the molar gas constant (8.314 J/(mol·K)), X_i is the mole fraction of the i-th substance ($X_{\mathrm{A}} + X_{\mathrm{B}} = 1$), and H_i is the molar heat of fusion (J/mol) of the i-th substance.

2.3 Preparation of hexadecanol-saturated diol EPCMs

The EPCMs composed of hexadecanol and three types of saturated diols were prepared using the melt blending method. Specifically, multiple batches of binary mixtures of hexadecanol and saturated diols, with varying mass ratios, were accurately weighed using an analytical balance and placed in separate beakers. These beakers were then immersed in a water bath magnetic stirrer for heating. Once the components had completely melted into a

homogeneous liquid phase, they were stirred at 400 rpm for 30 minutes to ensure uniform mixing. The water bath temperatures for preparing HD-ODL, HD-DDL, and HD-DDD EPCMs were set at 65 ℃, 75 ℃, and 85 ℃, respectively. After complete melting and mixing, the mixtures were allowed to crystallize naturally at room temperature. Finally, the solidified products were collected and finely ground using a mortar and pestle, resulting in the formation of binary EPCMs with varying mass proportions.

2.4 Preparation of HD-DDD CPCMs

A vacuum impregnation technique was employed to synthesize CPCMs. Initially, the synthesized HD–DDD was immersed in a magnetic stirring water bath maintained at 70 °C and heated until it completely melted. A specific amount of EG was then introduced into the mixture, which was stirred manually for 10 minutes to ensure uniform dispersion. To eliminate entrapped air within the EG pores and ensure complete PCM infiltration, the mixture was subsequently transferred to a vacuum oven and maintained at 70 ℃ for 6 h under a vacuum of 0.08–0.1 MPa [41, 42]. This pressure reduction effectively evacuates gas from the porous network and drives the liquid PCM into the micropores of the EG, thereby ensuring uniform loading and strong capillary confinement. For the preparation of PB-doped CPCMs, PB was first dispersed into the PCM by stirring at 400 rpm for 10 minutes, followed by the addition of EG. The formulations of different sample groups are presented in Table 1. The first five groups were designed to determine the optimal EG content, while the last three groups were PB-doped samples. The contents of each component were subsequently optimized through subsequent experiments.

Table 1. Sample group names and their formulations.

Sample number	Sample name	EPCM (g)	EG (g)	PB (g)	EPCM:EG:PB (mass ratio)
1	EG8	10	0.8	0	100:8:0
2	EG10	10	1.0	0	100:10:0
3	EG12	10	1.2	0	100:12:0
4	EG14	10	1.4	0	100:14:0
5	EG16	10	1.6	0	100:16:0
6	EG14PB5	10	1.4	0.5	100:14:5
7	EG14PB10	10	1.4	1.0	100:14:10
8	EG14PB15	10	1.4	1.5	100:14:15

2.5 Characterization

The phase change characteristics were measured using a differential scanning calorimeter (DSC3+, Mettler Toledo), with a heating and cooling rate of 10 ℃/min over the temperature range of 10–100 ℃, under a nitrogen flow of 50 ml/min to ensure precise temperature control. The phase change temperature was obtained by determining the intersection point between the tangent drawn at the steepest slope of the primary DSC peak and the extrapolated baseline. The degree of supercooling was defined as the difference between the melting and freezing temperatures.

The chemical functional groups of the samples were characterized using a Fourier-transform infrared spectrometer (FTIR, Nicolet 6700, Thermo Fisher Scientific) in the wavenumber range of 400–4000 cm^{-1}. The crystal structure was analyzed using an X-ray diffractometer (XRD, Ultima IV X, Rigaku Corporation) with a scanning rate of 10 °/min in the 2θ range of 10° to 60°. The morphology of the samples was characterized using a high-resolution field-emission scanning electron microscope (SEM, Apreo 2S HiVac, Thermo Fisher Scientific), with gold coating applied prior to imaging. Energy-dispersive X-ray spectroscopy (EDS) was employed to analyze the distribution of iron elements on the surface of PB-containing samples.

Thermal conductivity was measured at room temperature using a thermal constant analyzer (HotDisk, TPS500S, Hot Disk AB) employing the transient plane source method. Thermal stability was assessed using a thermogravimetric analyzer (TGA, SDT Q600, TA Instruments-Waters LLC) in a nitrogen atmosphere (100 ml/min) within the temperature range of 25–600 ℃. High and low-temperature cycling tests were conducted using a Bell Instruments thermal cycling chamber (BTH-80B) in the temperature range of 20–70 ℃, with up to 300 freeze-thaw cycles. The cycling stability of the samples was determined via DSC. The optical absorption properties of the samples were characterized in the 250–2500 nm range using a UV–Vis–NIR spectrophotometer (UV-3600 Plus, Shimadzu).

The photothermal conversion properties were evaluated using a CME-SL500 solar light simulator at an irradiance of 1000 W/m^2, coupled with a T-type thermocouple and a KEYSIGHT DAQ970A data acquisition instrument. The instrument accuracies are provided in Table 2.

Table 2. Instrument accuracy.

Instrument	Parameter	Unit	Accuracy
DSC	Enthalpy	kJ/kg	±3%
Hot Disk	Thermal conductivity	W/(m·K)	±5%
BTH-80B chamber	Temperature	℃	±0.5 ℃
TGA	Mass	mg	±0.001%
T-type thermocouple	Temperature	℃	±0.8 ℃
UV-Vis-NIR	Wavelength	nm	UV-Vis: ±0.2 nm NIR: ±0.8 nm
Data acquisition system	Time	s	Accuracy: 1 ms Resolution: 1 s
Analytical balance	Mass	g	0.001 g
Radiometer	Irradiance	W/m^2	±5%
Vernier caliper	Length	mm	0.01 mm

3. Results and discussion

3.1 Determination of the optimal eutectic point for binary eutectic mixtures

EPCM refers to a binary or multi-component mixture that is co-melted and exhibits high latent heat at the optimal eutectic point. The optimal eutectic point of the EPCM is determined through a combination of theoretical calculations and experimental methods. Initially, the binary eutectic phase diagrams of HD with ODL, DDL, and DDD were plotted using Equation (1). The DSC curves of the four PCMs and the calculated parameters are presented in Fig. 1(a) and Table 3, with the calculation results shown in Figs. 1(b) to (d). As shown in Fig. 1(a), the solidification curve of pure HD displays a distinct double peak, primarily due to the successive liquid-to-solid and solid-to-solid phase changes during HD solidification, with the solid-to-solid transition corresponding to a polymorphic transformation of HD [43]. By solving the intersection points of the saturation liquid phase lines for each binary pair, the molar fractions of HD at the theoretical eutectic points were determined to be 0.5390, 0.7119, and 0.8284, corresponding to mass percentages of 65.97%, 77.47%, and 85.27%, respectively.

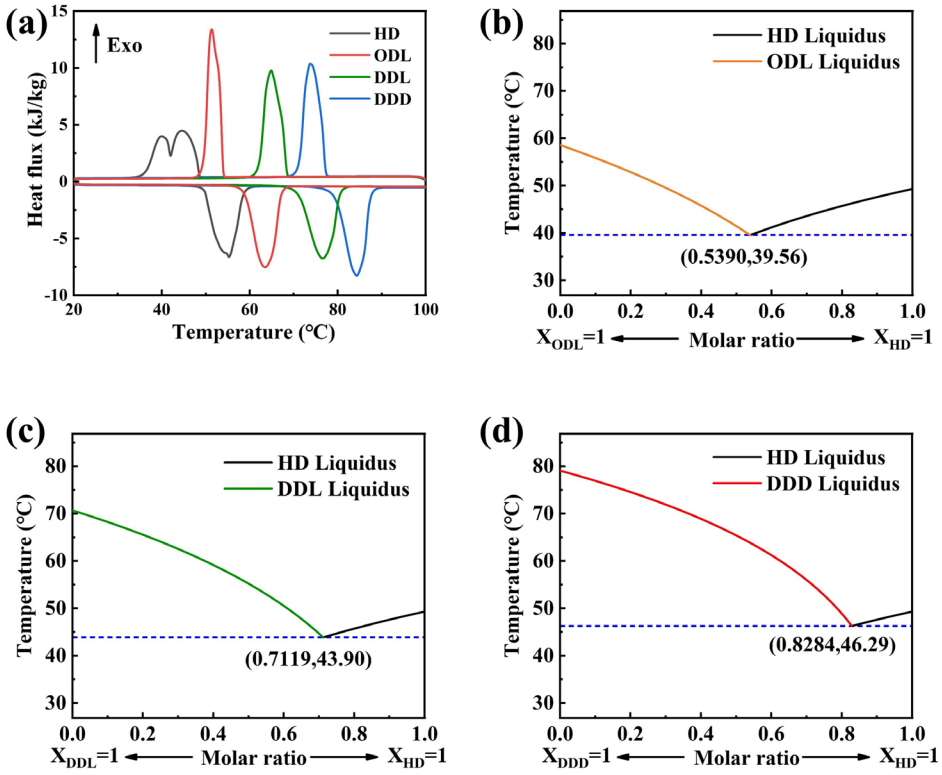

Fig. 1. (a) DSC curves of the PCMs, and predicted phase diagrams: (b) HD-ODL, (c) HD-DDL, (d) HD-DDD.

Table 3. Calculation parameters for the saturated liquid line.

PCM	Molecular weight	T_m (K)	H_m (kJ/kg)	H_m (J/mol)
HD	242.44	322.5	218.7	53021.6
ODL	146.23	331.7	240.2	35124.4
DDL	174.28	343.9	241.3	42053.8
DDD	202.33	352.3	248.7	50258.8

To further confirm the actual eutectic points of the three EPCMs, six different eutectic compositions near their theoretical eutectic points were prepared and tested by DSC. Figs. 2(a) to (f) present the DSC curves. All three EPCMs exhibited a single melting peak near their theoretical eutectic points, indicating an excellent compatibility between the saturated diols and HD. Notably, Figs. 2(b) and (c) illustrate that in the binary mixtures of HD with DDL and DDD, as the mass fraction of HD decreases, the solidification peaks of the binary mixtures progressively converge to a single peak, reflecting consistent crystallization behavior in the mixtures.

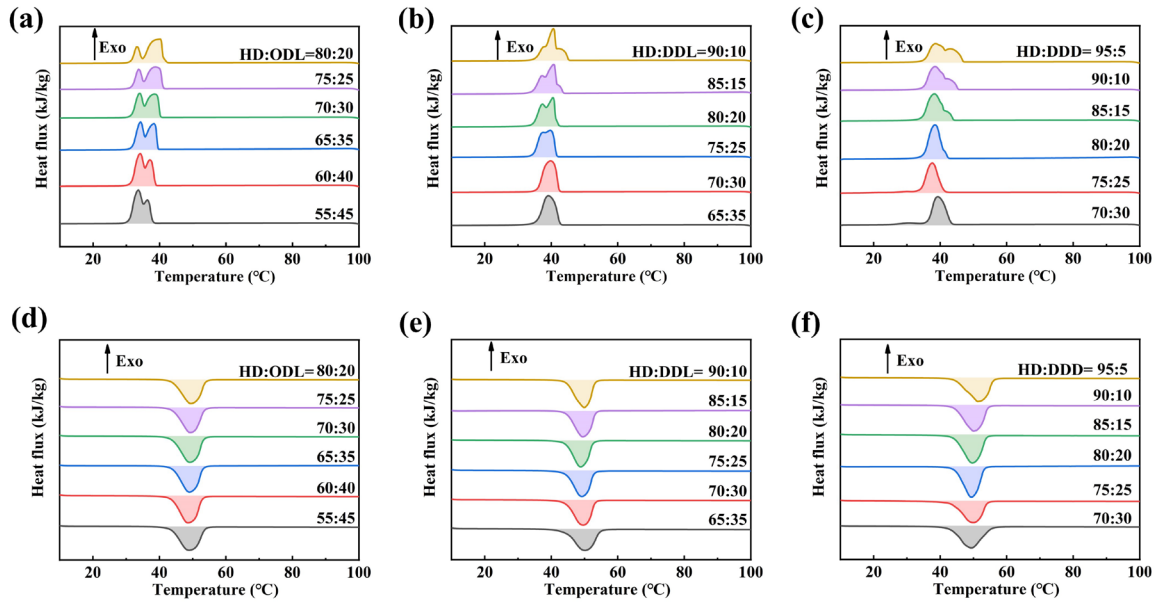

Fig. 2. DSC solidification curves at different eutectic ratios: (a) HD-ODL, (b) HD-DDL, (c) HD-DDD, and melting curves: (d) HD-ODL, (e) HD-DDL, (f) HD-DDD.

Three distinct EPCM systems, selected based on their high latent heat and low supercooling, are presented in Table 4. The experimentally determined mass fractions of HD at the eutectic points for the these three EPCMs were 70%, 70%, and 85%, respectively. These

values deviate from the theoretical predictions calculated using Equation (1) (65.97%, 77.47%, and 85.27%) by 4.03%, 7.47%, and 0.27%, respectively. These discrepancies can be primarily attributed to two factors. First, Equation (1) is derived from an ideal solution model that assumes zero excess enthalpy [8]. However real binary systems often exhibit non-ideal behavior due intermolecular interactions. Second, inherent experimental uncertainties associated with DSC measurements, such as baseline determination and heating rate effects, may contribute to minor variations in the identified eutectic composition. Despite these minor deviations, Equation (1) remains a reliable theoretical tool for predicting eutectic compositions, providing a preliminary basis for experimental design and significantly reducing the experiments required to identify optimal formulations [44].

Table 4. Optimal eutectic ratios of three EPCMs and comparison with literature.

PCM	H_m (kJ/kg)	H_f (kJ/kg)	T_m (°C)	T_f (°C)	ΔT_s (°C)	Refs.
LA	175.8	NA	44	NA	NA	[46]
MA:SA = 64:36	182.4	NA	44.1	NA	NA	[47]
MA:PA = 66.92:33.08	183.1	185.6	45.36	43.80	1.56	[9]
MA:SA = 66.92:33.08	180.6	177.3	46.41	42.09	4.32	[9]
MA:PW = 62:38	171.42	174.56	41.99	38.56	3.43	[48]
LA:HD = 60.17:39.83	200	NA	47.6	41.8	5.8	[49]
HD:ODL = 70:30	213.9	209.2	43.5	40.5	3	Present
HD:DDL = 70:30	214.8	212.9	44.0	42.7	1.3	Present
HD:DDD = 85:15	223.8	220.3	44.0	43.7	0.3	Present

All three EPCMs exhibited suitable melting points and latent heat advantages compared to other bio-based PCMs in the same temperature range, underscoring their potential for applications in low-temperature solar thermal energy utilization. Notably, the EPCM with a composition of HD:DDD = 85:15 demonstrated the highest latent heat and lowest supercooling, making it the optimal candidate for further study.

In addition, the thermal expansion coefficient (α) of the optimal EPCM was examined using Equation (2)[45].

$$\alpha = (V_2 - V_1)/[V_1(T_2 - T_1)] \quad (2)$$

where V_1 and V_2 are the volumes of the EPCM at temperatures T_1 and T_2, respectively. Specifically, the thermal expansion coefficient of the EPCM was estimated by measuring its volume in the solid state at T_1 = 20 ℃ and in the liquid state at T_2 = 80 ℃. The calculated α value was 2.79×10^{-3} $℃^{-1}$, which aligns well with values reported for bio-based EPCMs in the literature [45].

3.2 Chemical composition and crystal structure of EPCM

FTIR and XRD analyses were conducted to investigate the chemical composition and crystal structure of the HD-DDD, as presented in Fig. 3. As shown in the FTIR spectra, both HD and DDD exhibit a broad and intense absorption band centered at approximately 3300 cm^{-1}, which is attributed to the O–H stretching vibration of alcohol groups. The absorption bands at 2929 and 2842 cm^{-1} are assigned to the asymmetric and symmetric stretching vibrations of CH_2 groups, respectively. In addition, the bands observed at 1461 and 725 cm^{-1} are associated with the in-plane and out-of-plane deformation vibrations of the O–H group in alcohols. The peak at 1058 cm^{-1} is attributed to the C-O stretching vibration [43]. These characteristic peaks are also present in the FTIR spectrum of HD-DDD, indicating that the eutectic mixture of HD and DDD is merely a physical blend, without any chemical transformations occurring. XRD analysis was further employed to examine the crystal structure of HD-DDD, revealing three main diffraction peaks at 2θ = 22.0°, 23.1°, and 24.9°, which correspond to the strong diffraction peaks of HD and DDD. This suggests that the eutectic process does not alter the crystal structure of the individual components, preserving their structural integrity.

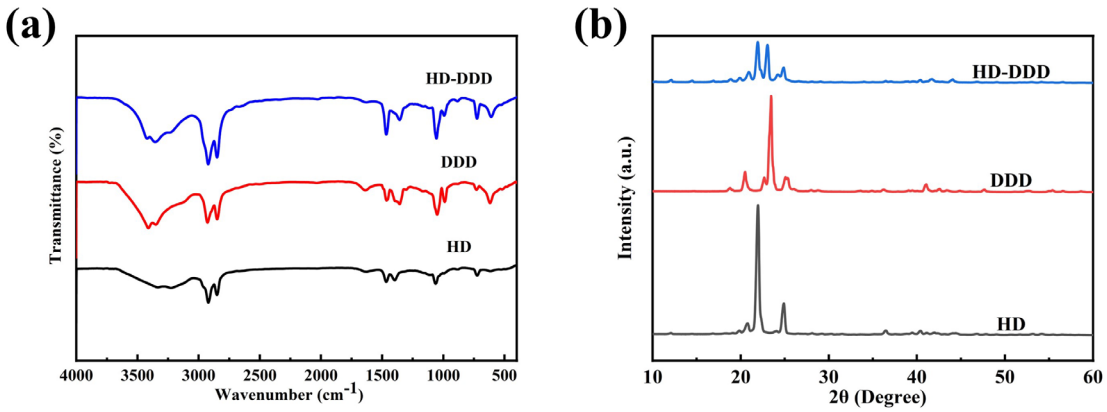

Fig. 3. (a) FTIR spectra and (b) XRD patterns of HD, DDD, HD-DDD.

3.3 Leakage tests and micromorphology of CPCMs

Pure PCMs are prone to leakage during application, which can compromise their thermal storage performance. To address this issue, a shape-stable CPCM was prepared by incorporating EG into the pure phase change material HD-DDD. Shape stability is essential for preventing liquid-phase leakage and ensuring the retention of high thermal storage and release capacity during use. Fig. 4 presents the microscopic morphology of EG, EG14, and EG14PB10, respectively. As observed, EG exhibits a worm-like morphology with internally layered micropores, which provide adequate capillary forces for the adsorption of liquid PCM. In both EG14 and EG14PB10, the micropores of EG are fully infiltrated with PCM. Furthermore, iron element mapping images confirm that PB was successfully coated onto the EG14PB10 sample. In addition, EDS mapping was performed on the three samples with varying PB contents. As shown in Figs. 5(d)–(f), the Fe signal is uniformly distributed across the entire scanned region in all cases, with no evidence of Fe-rich domains or large-scale agglomerates. These results confirm PB remains well dispersed within the EG scaffold across different loadings, without significant macroscopic agglomeration.

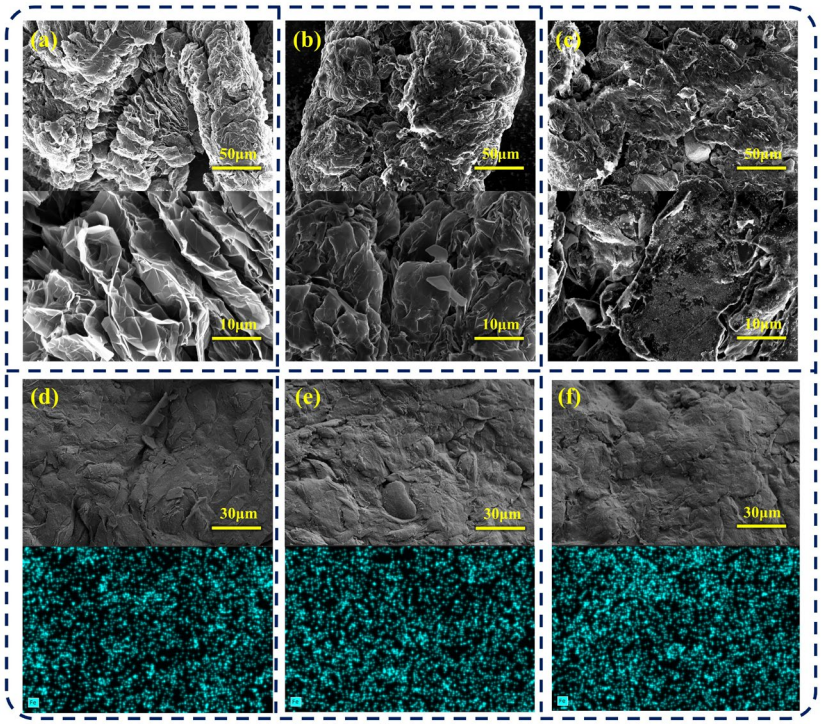

Fig. 4. SEM images of (a) EG, (b) EG14, (c) EG14PB10 and iron elemental mapping images of (d) EG14PB5, (e) EG14PB10, (f) EG14PB15.

Increasing the EG content enhances the adsorption capacity of the PCM. However, excessive EG content significantly reduces the latent heat of the CPCM. Therefore, an anti-leakage experiment was conducted to optimize the EG content, ensuring that the CPCM retains high latent heat while maintaining good shape stability. In this experiment, the prepared CPCM was compressed into cylindrical samples and subjected to continuous heating at 70 ℃ for 24 h. The optimal EG content was determined by observing the traces of PCM left on filter paper and measuring the mass loss ratio, which was calculated using Equation (3).

$$M_{loss} = [(m_1 - m_2)/m_1] \times 100\% \quad (3)$$

where m_1 is the initial mass, m_2 is the mass after heating, and M_{loss} is the mass loss percentage. The results of the anti-leakage experiment are presented in Fig. 5(a). After 30 minutes of heating, PCM leakage was observed in sample EG8-12, while no significant leakage was detected in samples EG14, EG16, and EG14PB10. The mass loss ratios for the six sample groups presented in Fig. 5(b) were 3.44%, 1.36%, 0.83%, 0.26%, 0.25%, and 0.10%, respectively. Both experiments indicate that when the mass ratio of EG to EPCM is 100:14, the CPCM does not experience leakage during the phase change process. Moreover, the mass loss rate for the PB-doped sample with 1.4 g of EG was further reduced, possibly attributed to the inherent pore structure of PB [50], which further enhances the anti-leakage performance. After 24 h of continuous heating, visual inspection of the filter papers beneath the samples revealed significant differences in leakage behavior. The filter papers under EG8 and EG10 were almost completely saturated with leaked PCM, indicating poor shape stability. In contrast, no visible liquid leakage was observed for EG14, EG16, or EG14PB10. These observations were corroborated by quantitative mass loss measurements, which yielded values of 6.19%, 2.19%, 0.90%, 0.29%, 0.27%, and 0.28% for the respective samples (e.g., EG8, EG10, EG12, EG14, EG16, EG14PB10]. Notably, both samples EG14 and EG14PB10 exhibited negligible mass loss (<0.3%), demonstrating excellent leakage resistance under high temperature conditions.

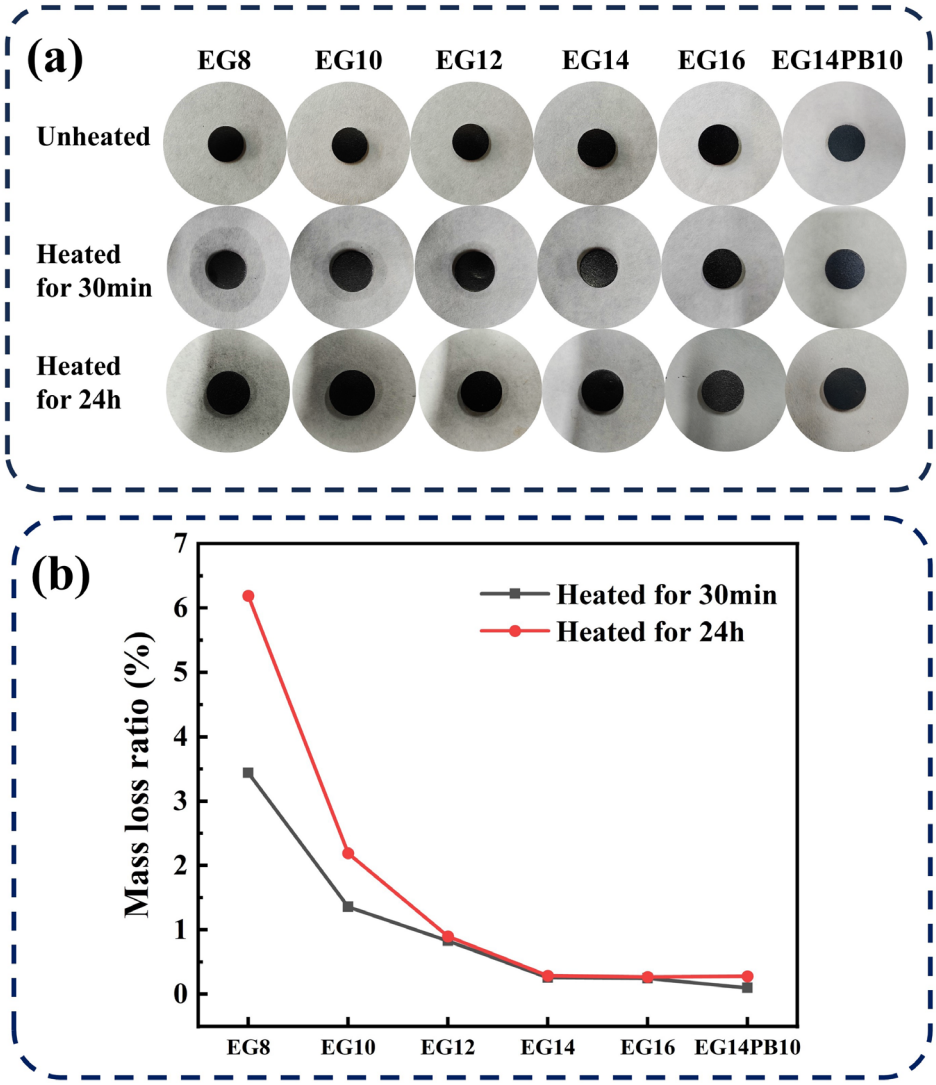

Fig. 5. Comparative analysis of the samples: (a) visual appearance before and after heating, (b) percentage mass loss post-heating.

Furthermore, the mass loss ratios of EG14, EG16, and EG14PB10 increased only marginally after 24 h of heating compared to 30 min, indicating that PCM adsorption by EG had reached saturation. This confirms the long-term shape stability of the samples.

3.4 Light absorption characteristics of CPCMs

Photothermal PCMs convert light into heat by absorbing solar radiation, thereby driving the phase change process for thermal energy storage. Their performance is predominantly governed by their ability to harvest the solar spectrum [19]. The UV-Vis-NIR absorption spectra of HD-DDD, EG14, EG14PB5, EG14PB10, and EG14PB15 are shown in Fig. 6. Pure HD-DDD, a eutectic PCM, exhibits negligible absorption across the entire solar spectrum,

confirming that unmodified PCMs are inherently unsuitable for direct solar thermal applications.

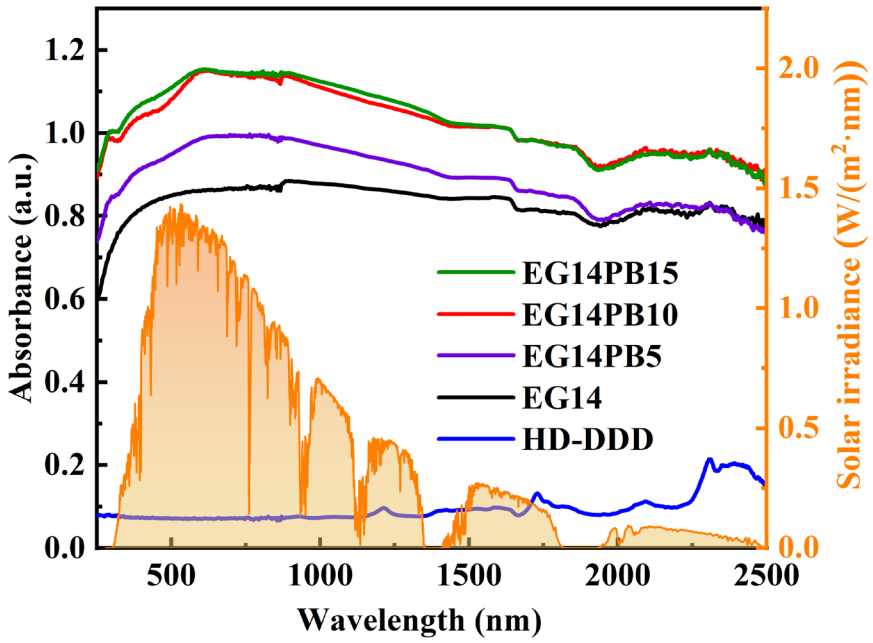

Fig. 6. UV–Vis-NIR absorption spectrum of CPCMs.

The incorporation of EG significantly enhances light absorption across the 250–2500 nm range, with the most pronounced improvements occurring in the visible and NIR regions. This enhancement stems from loosely bound π-electron structure of EG, which is readily excited by a wide range of photon energies and efficiently dissipates the excess energy as heat, enabling effective photothermal conversion [33].

The incorporation of PB further increases absorption across the entire solar spectrum through the synergistic interaction between EG and PB. Notably, PB-containing composites show the greatest absorption enhancement in the 380–1000 nm range, the most energy-rich portion of sunlight, compared to EG14 alone. Specifically, the average absorption increases in this region are 10.4–15.2% for EG14PB5, 25.4–33.5% for EG14PB10, and 28.0–33.9% for EG14PB15. This improvement is attributed to ligand-to-metal charge transfer transitions between Fe^{2+} and Fe^{3+} ions in PB, which are particularly active within this wavelength window [51]. These findings corroborate that PB, with its strong NIR absorption, effectively complements the broad-spectrum light-harvesting capability of carbon-based materials such as EG [34]. Compared with EG14PB5, EG14PB10 exhibited a significantly enhanced absorbance, which is attributed to the increased density of light-absorbing sites from the increased PB

loading. However, at a mass ratio of EPCM:EG:PB = 100:14:15 (i.e., EG14PB15), no further increase in absorbance was observed, despite the maintained uniform PB dispersion. This phenomenon is likely due to the saturation of PB within the composite, which limits additional gains in light harvesting.

Overall, the EG-PB hybrid architecture demonstrates substantially enhanced solar absorption, highlighting its strong potential for solar thermal energy storage. Although EG14PB15 achieves slightly higher absorbance than EG14PB10, the improvement is marginal. Moreover, since PB itself does not undergo a phase change, excessive PB loading reduces the mass fraction of the PCM, thereby compromising the latent heat of the composite. Consequently, EG14PB10 was selected for subsequent studies, as it offers an optimal balance between high solar absorption and high latent heat storage capacity.

3.5 Chemical composition and crystal structure of CPCMs

FTIR and XRD analyses were conducted to evaluate the chemical composition and crystal structure of the CPCMs, with the results presented in Fig. 7. In the FTIR spectrum of EG, a broad peak at 3300 cm^{-1} and a characteristic peak at 1632 cm^{-1} correspond to the stretching vibrations of O-H and C-O, respectively [13]. For PB, the stretching vibration peaks of the C≡N bond and the Fe^{2+}-CN-Fe^{3+} groups were observed at 2096 cm^{-1} and 499 cm^{-1}, respectively [35]. Notably, the FTIR spectra of EG14 and EG14PB10 reflect combinations of the spectra of the individual components, with a decrease in peak intensity, indicating a reduction in the content of the corresponding materials. Therefore, these results suggest that the preparation of CPCMs is a purely physical process, with no chemical reactions occurring.

XRD analysis was further employed to investigate the crystal structure of the CPCMs. In both composite materials, the characteristic peak (002) of EG at $2\theta = 26.6°$ and the characteristic peaks of HD-DDD at $2\theta = 22.0°$, 23.1°, and 24.9° were observed. Additionally, four distinct diffraction peaks of PB at $2\theta = 17.4°$, 24.7°, 35.6°, and 39.5° were detected, with corresponding peaks also presented in the diffraction pattern of the EG14PB10 sample. These XRD results confirm that the addition of EG and PB does not alter the crystal integrity of HD-DDD, further supporting the conclusion that the preparation of CPCMs involves only physical mixing, consistent with the FTIR analysis.

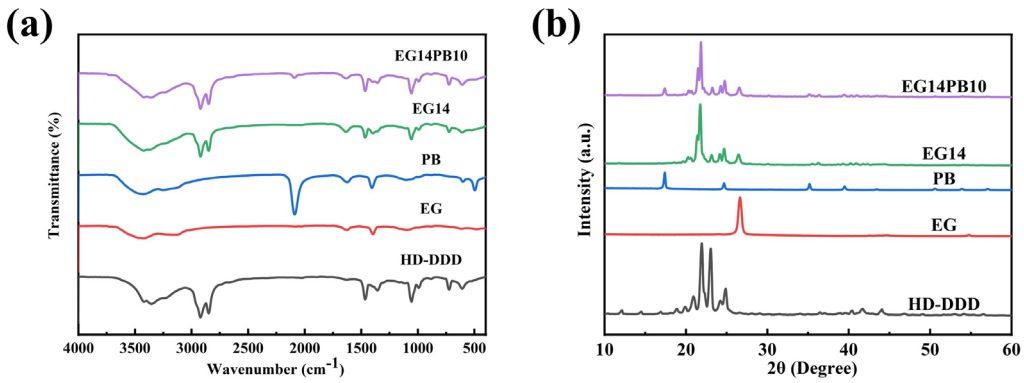

Fig. 7. (a) FTIR spectra and (b) XRD patterns of HD-DDD, EG, PB, EG14, EG14PB10.

3.6 Phase change behavior and thermal conductivity of CPCMs

As a fundamental thermophysical property, thermal conductivity plays a decisive role in controlling heat transfer processes in PCMs, which is crucial for their performance in thermal energy storage systems. As presented in Fig. 8(a), the pristine phase change material, HD-DDD, exhibits inherently poor heat transport capability, with a measured thermal conductivity of only 0.39 W/(m·K), making it unsuitable for practical applications. By contrast, the incorporation of EG resulted in a pronounced enhancement in the thermal conductivity of the CPCMs, which increased to 6.10, 8.26, 8.94, and 9.75 W/(m·K) with increasing EG loading. Among them, the thermal conductivity of EG14 is 25.0 times higher than that of HD-DDD. This significant enhancement is attributed to the formation of a three-dimensional heat conduction network upon EG addition [52], which enables rapid heat transfer. Furthermore, the thermal conductivity of EG14PB10 attains 9.62 W/(m·K), approximately 24.7 times that of HD-DDD, indicating that the addition of 1.0 g of PB does not disrupt the heat conduction network established by EG.

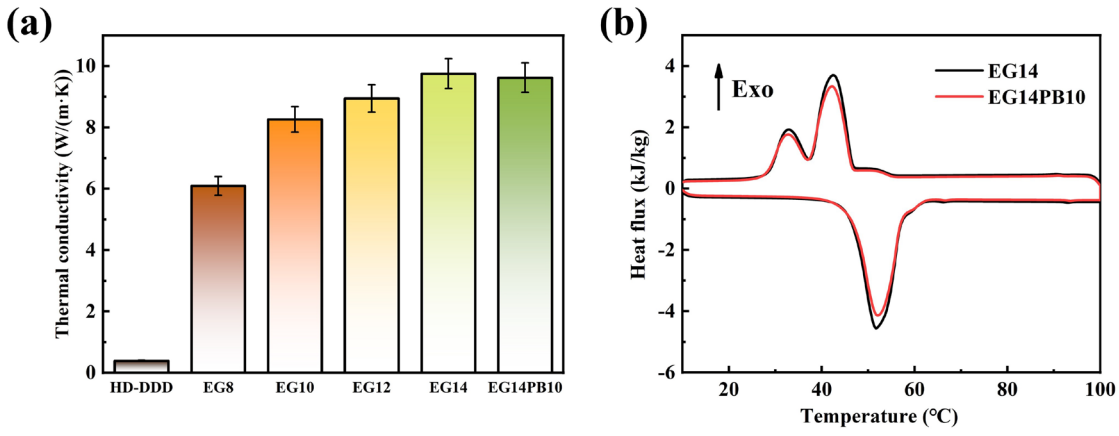

Fig. 8. (a) Thermal conductivity of CPCMs and (b) DSC curves of EG14 and EG14PB10.

DSC was employed to characterize the phase change behavior of EG14 and EG14PB10. Based on the DSC curves, the melting temperatures of the two materials were identified as 46.2 ℃ and 46.3 ℃, respectively, with corresponding melting enthalpies of 191.3 kJ/kg and 180.6 kJ/kg. The freezing points were 47.0 ℃ and 46.9 ℃, with freezing enthalpies of 198.4 kJ/kg and 177.4 kJ/kg, respectively. Since EG and PB do not undergo phase changes within the DSC test temperature range, the enthalpy deviation of the CPCMs from the theoretical enthalpy can be calculated using Equation (4).

$$\delta = |(\omega H_{\mathrm{PCM}} - H_{\mathrm{m}})/(\omega H_{\mathrm{PCM}})| \times 100\% \quad (4)$$

where δ represents the enthalpy percentage deviation, H_{m} is the measured enthalpy of the CPCM, H_{PCM} is the enthalpy of the original PCM, and ω is the mass fraction of PCM in the CPCM. The calculated deviations of the melting enthalpy for EG14 and EG14PB10 from the theoretical values were 2.55% and 0.05%, respectively, indicating that the vacuum impregnation method effectively maximizes PCM adsorption and ensures its uniform distribution. Notably, after the addition of EG, the freezing peak of the CPCM exhibited a double peak, and the melting point showed a slight shift compared to HD-DDD. This behavior is primarily ascribed to the porous architecture of EG, which imposes a confinement effect on the PCM. The structure limits the volume expansion of the PCM during phase changes, creating increased pressure within the pores and influencing the thermodynamic behavior of the material [20]. Nevertheless, the melting peaks of both EG14 and EG14PB10 remain as single peaks, confirming that their eutectic structure is preserved.

3.7 Thermal stability and cycling stability of CPCMs

Thermal stability testing is essential for determining the safe operating temperature range of CPCMs, providing critical data for their practical application. The thermal stability of the materials was assessed using TGA. The TGA curves for HD-DDD, EG14, and EG14PB10 are presented in Fig. 9. The starting thermal decomposition temperature is defined as the temperature at which a 5% mass loss occurs [53]. The starting thermal decomposition temperature of HD-DDD is 204.4 ℃, while both EG14 and EG14PB10 exhibit a higher starting thermal decomposition temperature of 220.9 ℃, which is 16.5 ℃ higher than that of HD-DDD. This enhancement suggests that the porous encapsulation provided by EG effectively retards

the thermal degradation of the PCM. Notably, both EG14 and EG14PB10 retain some residual mass at 600 ℃, which is primarily due to the fact that EG does not undergo thermal decomposition at this temperature in a nitrogen atmosphere [13]. Additionally, a minor mass loss between approximately 300–450 ℃ in EG14PB10 is attributed to the release of cyano groups from PB [54]. Overall, the thermal decomposition temperatures of EG14 and EG14PB10 are significantly higher than the operational temperature range of the PCMs, confirming their excellent thermal stability.

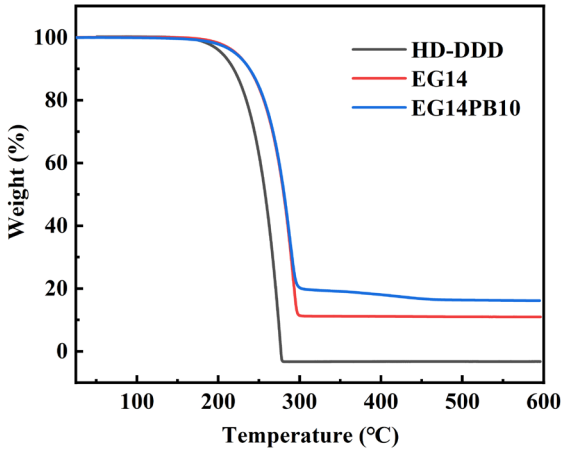

Fig. 9. TGA curves of HD-DDD, EG14 and EG14PB10.

Cyclic stability is critical for ensuring the long-term performance of PCMs. The heat absorption and release curves of EG14 and EG14PB10 after 150 and 300 thermal cycles were obtained using DSC, as shown in Figs. 10(a) and (b). The DSC curves after thermal cycling are nearly identical to those obtained before cycling, indicating that the phase change behavior of both CPCMs remains unchanged. After 150 cycles, the melting enthalpy of EG14 and EG14PB10 slightly increased, likely due to experimental uncertainty. After 300 cycles, the melting enthalpies of the two CPCMs decreased by only 1.4% and 3.0%, respectively, compared to the pre-cycled values. Furthermore, as shown in Table 5, the incorporation of EG significantly reduces the supercooling degree (ΔT_s) compared to pristine HD–DDD (0.3 ℃). This reduction can be attributed to the abundant layered porous structure of EG, which provides numerous heterogeneous nucleation sites that facilitate PCM solidification [13]. Moreover, the supercooling degree of the CPCMs remains virtually unchanged after thermal cycling, suggesting that the nucleation-promoting effect of EG is robust and well-preserved throughout repeated phase change process. To further assess the structural integrity, the chemical

composition and crystal structure of EG14 and EG14PB10 before and after 300 cycles were analyzed using FTIR and XRD, as presented in Figs. 10(c) and (d). The results show no significant changes in the FTIR and XRD spectra, with no shifts or alterations in the peak shapes before and after cycling. The results confirm that no significant changes occur in the chemical composition or crystalline structure of EG14 and EG14PB10 after 300 thermal cycles, highlighting the excellent thermal cycling stability of both CPCMs.

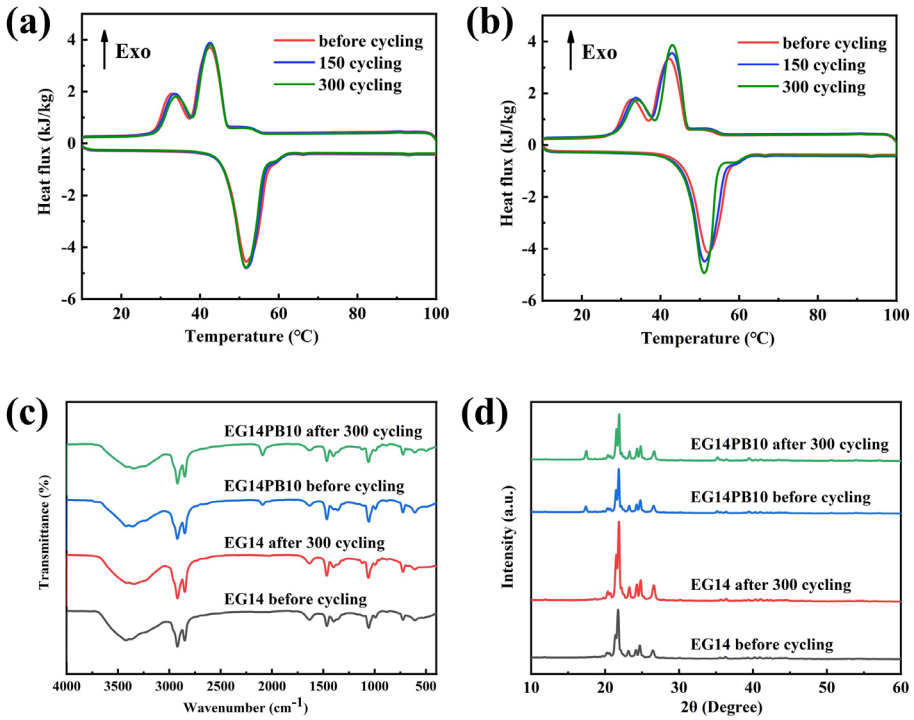

Fig. 10. DSC curves of (a) EG14 and (b) EG14PB10 before and after 300 cycles, (c) FTIR spectra and (d) XRD patterns of EG14 and EG14PB10 before and after 300 cycles.

Table 5. Phase change properties of EG14 and EG14PB10 after 300 freeze–thaw cycles.

Sample	Cycle	H_m (kJ/kg)	Change in H_m	H_f (kJ/kg)	Change in H_f	T_m (°C)	Change in T_m (°C)	T_f (°C)	Change in T_f (°C)	ΔT_s (°C)
EG14	1	191.3	0.0%	189.4	0.0%	46.2	0.0	47.0	0.0	-0.8
	150	192.5	0.6%	192.0	1.4%	46.2	0.0	47.1	0.1	-0.9
	300	188.6	-1.4%	184.2	-2.7%	46.2	0.0	47.0	0.0	-0.8
EG14P B10	1	180.6	0.0%	177.8	0.0%	46.3	0.0	46.9	0.0	-0.6
	150	181.3	0.4%	181.4	2.0%	46.2	-0.1	47.1	0.2	-0.9

300	175.2	-3.0%	173.4	-2.5%	46.1	-0.2	47.0	0.1	-0.9

3.8 Photothermal conversion characteristics of CPCMs

To investigate the photothermal conversion characteristics of CPCMs under light conditions, the photothermal characteristics of EG14 and EG14PB10 were measured using the setup presented in Fig. 11(a). A xenon lamp was used as the light source, which irradiated the surface of the samples, while a T-type thermocouple measured the temperature of the samples. Data acquisition instrument recorded the temperature changes over time, and the results are shown in Fig. 11(b). Initially, both EG14 and EG14PB10 experienced a rapid increase in temperature, which then slowed, followed by a distinct plateau on the photothermal conversion curve. This plateau indicates that the PCM inside the CPCMs undergoes a solid-liquid phase change and stores thermal energy. Once the light source was switched off, a rapid temperature decline was observed for both samples due to the release of the stored heat. Notably, EG14PB10 completed the phase change significantly faster than EG14 and reached a temperature of 6.3 ℃ higher than EG14 at the end of irradiation, demonstrating superior photothermal performance. Such an enhancement originates from the synergistic effect of EG and PB, which is consistent with the UV–Vis–NIR results. The photothermal conversion efficiency of the CPCMs was calculated using the formula (5) [55].

$$\eta = mH_{\mathrm{m}}/[IS(t_2 - t_1)] \quad (5)$$

where η is the photothermal conversion efficiency, m and H_{m} are the sample mass and melting enthalpy, I is the light intensity, measured by a light power density meter, S is the illuminated area, and t_2 and t_1 are the times corresponding to the completion and start of the phase change, respectively. Time intervals were recorded using a data acquisition system, while the illuminated area was determined from dimensions measured with a vernier caliper. The uncertainties associated with these parameters are summarized in Table 2. It is important to note that Equation (5) is specifically used to calculate the solar energy conversion efficiency during the phase change process for phase change energy storage. The calculated photothermal conversion efficiencies of EG14 and EG14PB10 are 83.4% and 93.7%, respectively. Compared to EG14, the photothermal conversion efficiency of EG14PB10 increased by 10.3%, while the

latent heat decreased by only 5.6%. The superior photothermal performance arises from two synergistic mechanisms. First, the spectral absorption capabilities of the components are complementary. While EG provides broad-spectrum light absorption across the ultraviolet, visible, and NIR regions via its delocalized π-electron structure, PB introduces strong, selective absorption in the visible to NIR region (380–1000 nm). This enhanced absorption is attributed to ligand-to-metal charge transfer transitions between Fe^{2+} and Fe^{3+} ions within the PB framework [51]. Consequently, PB effectively supplements the absorption profile of EG, particularly in the high-energy visible region where solar irradiance is most intense. Second, the structural and thermal properties of the EG scaffold further enhance efficiency. The highly porous network of EG offers a large specific surface area, maximizing the exposure of light-absorbing sites. Furthermore, the high thermal conductivity of EG facilitates rapid transfer of photogenerated heat from PB to the surrounding PCM. This efficient heat transfer minimizes heat loss and accelerates the phase transition process, thereby enhancing the overall photothermal conversion performance.

Table 6 compares the performance of EG-based CPCMs and bio-based EPCM-based reported in previous studies with the results of this work. Due to the high latent heat of HD-DDD, the high thermal conductivity of EG, and the excellent light absorption properties resulting from the combination of EG and PB, the EG14PB10 composite phase change material developed in this study demonstrates comprehensive performance advantage. Beyond the demonstrated thermal and photothermal performance, the practical viability of the EG14PB10 composite is further supported by its potential for scalable manufacturing. The constituent materials, HD, DDD, EG, and PB, are commercially available and cost-effective [32, 56]. The fabrication protocol is straightforward, involving only the melt blending of the eutectic PCM followed by vacuum impregnation with EG and a PB dispersion. This approach avoids the need for specialized equipment or complex synthesis steps, ensuring compatibility with existing industrial production lines. Considering the favorable balance between low material cost, processing simplicity, and significant performance enhancements, EG14PB10 exhibits substantial potential for practical low-temperature solar thermal energy storage applications.

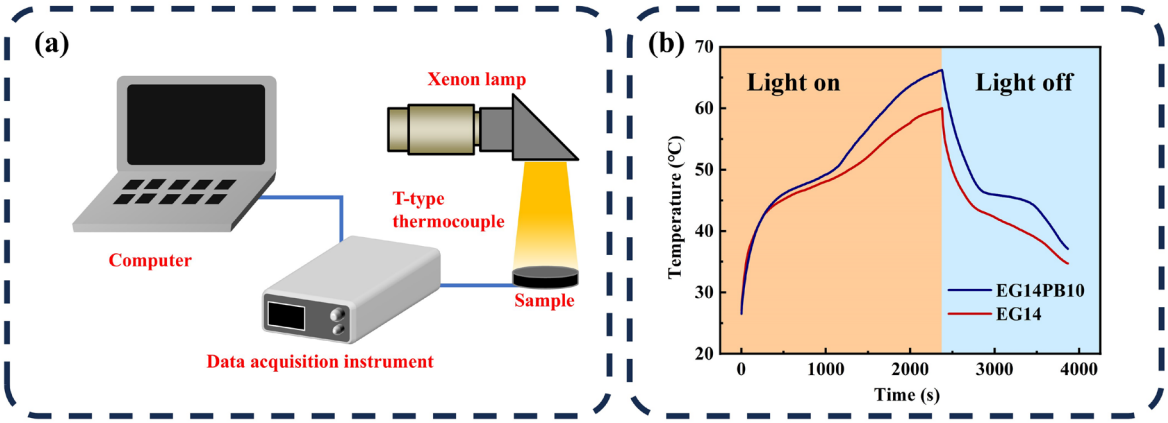

Fig. 11. (a) Photothermal device schematic diagram, (b) Photothermal conversion curves of EG14 and EG14PB10.

Table 6. Comparison of performance between the present work and reported EG-based and bio-based EPCM composites.

PCM	Skeleton	H_m (kJ/kg)	Thermal conductivity (W/(m·K))	η (%)	Refs.
PW	EG/BCN nanospheres	185.4	1.611	92.6	[55]
PA	EG/AgNPs	130.5	2.987	86.0	[57]
PW	EG/triazine	111.26	4.5488	86.9	[58]
PEG	EG/Cu-Zn-MOF	174.6	6.096	88.69	[59]
PW	EG/ZIF-67	159.2	0.93	95.56	[60]
PW	EG/polyolefin elastomer	142.8	1.929	93	[61]
LA-SA	CNTs/GO/PVA carbon aerogel	141.3	1.26	87.6	[62]
LA-MA	rGCA/LMG	124.6	NA	96.5	[63]
LA-SA	Carbon-decorated diatomite	70.07	0.38	94.83	[64]
HD-DDD	EG	191.3	9.75	83.4	Present
HD-DDD	EG/PB	180.6	9.62	93.7	Present

4. Conclusions

This study presents the preparation of three novel bio-based EPCMs, namely HD-ODL, HD-DDL, and HD-DDD, through a combination of theoretical calculations and experimental

methods. Among these, the HD:DDD=85:15 composition exhibited the highest latent heat and negligible supercooling, offering a latent heat advantage over other bio-based PCMs in the same temperature range. The subsequent fabrication of shape-stable CPCMs via vacuum impregnation with EG and PB enabled a synergistic enhancement of thermal and photothermal properties. Based on this study, the following conclusions can be drawn:

(1) The optimal contents of EG and PB were determined through leakage resistance tests and UV-Vis-NIR measurements, with the mass ratio of EPCM:EG:PB optimized to 100:14:10.

(2) The optimized EG14PB10 composite exemplifies the benefits of this design strategy: the porous EG network ensures rapid heat transfer and structural stability, while the PB coating broadens solar absorption, achieving exceptional photothermal conversion efficiency without significantly compromising latent heat. EG14PB10 exhibits a melting point of 46.3 ℃, a high latent heat of 180.6 kJ/kg, a significantly enhanced thermal conductivity of 9.62 W/(m·K) (24.7 times that of HD-DDD), and an elevated thermal decomposition temperature of 220.9 ℃, demonstrating its superior heat storage capability in various applications. EG14PB10 maintains its phase change behavior, chemical composition, and crystal structure after 300 thermal cycles, with only a 3.0% reduction in latent heat, demonstrating outstanding thermal stability and cycling durability.

(3) The incorporation of PB significantly enhances the solar absorption capacity of EG14PB10 across the full spectrum. Consequently, EG14PB10 achieves a photothermal conversion efficiency of 93.7%, representing a 10.3% improvement over EG14, while exhibiting only a 5.6% reduction in latent heat. This enhanced performance is attributed to two synergistic factors: complementary spectral absorption between PB and EG, and the porous EG network which facilitates efficient heat transfer.

Beyond material performance metrics, this work demonstrates a holistic strategy for engineering multifunctional CPCMs that balance energy storage capacity, thermal conductivity, photothermal efficiency, and long-term stability. The EG14PB10 composite represents a promising candidate for practical applications in low-temperature solar energy harvesting, building thermal regulation, and sustainable energy systems, providing a blueprint for the rational design of next-generation bio-based PCMs.

While this study focused on hexadecanol blended with specific diols (ODL, DDL, and DDD), future work could expand this scope to include a broader range of bio-based alcohols or multi-component alcohol systems. Such investigations would allow for precise tuning of phase change temperatures and further optimization of thermophysical properties, which are critically dependent on component selection and stoichiometry. Additionally, although the optimal EPCM:EG:PB ratio (100:14:10) was identified based on thermal and photothermal performance in this study, future studies could systematically explore composition optimization from a techno-economic perspective. Specifically, future efforts should aim to minimize material cost while maintaining high latent heat, thermal conductivity, and photothermal efficiency, a balance that is essential for the successful large-scale applications of these materials.

CRediT authorship contribution statement

Wenke Cheng: Investigation, Methodology, Writing-original draft. **Songping Mo**: Conceptualization, Funding acquisition, Project administration, Supervision, Writing-review & editing. **Kai Fu**: Investigation. **Yanping Du**: Writing-review & editing. **Zhi Yang**: Writing-review & editing. **Lisi Jia**: Writing-review & editing. **Ying Chen**: Resources.

Declaration of Competing Interests

The authors declare no competing financial interest.

Data availability

Data will be made available on request.

Acknowledgments

This work was supported by the Natural Science Foundation of Guangdong Province, China (Grant No. 2026A1515010683).

References

[1] Y. Liu, X. Cao, M. Yang, M. Wei, J. Mao, J. Sun, H. Xiang, H. Wang, Flame-retardant wood-based composite phase change materials based on polydopamine functionalized carbon dots for efficient solar-to-thermal energy storage, Adv. Compos. Hybrid Mater. 8 (2025) 1-22. https://doi.org/10.1007/s42114-025-01467-y.

[2] F. Pusponegoro, A.M. Fathoni, D. Agustina, T.M.I. Mahlia, N. Putra, Thermal performance and techno-economic analysis of passive cooling for photovoltaic panel using Phase Change Material (PCM) in the tropics, Results Eng. 28 (2025) 107547. https://doi.org/10.1016/j.rineng.2025.107547.

[3] M. Han, L. Lu, Phase change materials integrated into building envelopes for thermal management: A review, J. Build. Eng. 103 (2025) 112063. https://doi.org/10.1016/j.jobe.2025.112063.

[4] D. Paul, N. Biswas, S. Bhattacharyya, S. Alshehery, H. Togun, M.A. Alreshidi, K. K. Yadav, A comprehensive review on composite phase change materials for sustainable thermal energy solutions: Advances and barriers, Sustain. Mater. Technol. 45 (2025) e01578. https://doi.org/10.1016/j.susmat.2025.e01578.

[5] H. Togun, A. Basem, H.I. Mohammed, N. Biswas, A.M. Abed, F.L. Rashid, H.A. Maarof, J.D. Hamdi, A.K. Hussein, P. Paul, Harnessing solar energy with phase change materials: A review of melting point impacts, Int. Commun. Heat Mass Transf. 165 (2025) 109094. https://doi.org/10.1016/j.icheatmasstransfer.2025.109094.

[6] G. Suaria, S. Aliani, S. Merlino, M. Abbate, The Occurrence of Paraffin and Other Petroleum Waxes in the Marine Environment : A Review of the Current Legislative Framework and Shipping Operational Practices, Front. Mar. Sci. 5 (2018) 94. https://doi.org/10.3389/fmars.2018.00094.

[7] G. Simonsen, R. Ravotti, P. O'Neill, A. Stamatiou, Biobased phase change materials in energy storage and thermal management technologies, Renew. Sust. Energ. Rev. 184 (2023) 113546. https://doi.org/10.1016/j.rser.2023.113546.

[8] A. Anand, M. Mansor, K. Sharma, A. Shukla, A. Sharma, M.I.H. Siddiqui, K.K. Sadasivuni, N. Priyadarshi, B. Twala, A comprehensive review on eutectic phase change materials: Development, thermophysical properties, thermal stability, reliability, and applications, Alex. Eng. J. 112 (2025) 254-280. https://doi.org/10.1016/j.aej.2024.10.054.

[9] H. Ke, Phase diagrams, eutectic mass ratios and thermal energy storage properties of multiple fatty acid eutectics as novel solid-liquid phase change materials for sto

rage and retrieval of thermal energy, Appl. Therm. Eng. 113 (2017) 1319-1331. https://doi.org/10.1016/j.applthermaleng.2016.11.158.

[10] R. Kumar, S. Vyas, A. Dixit, Fatty acids/1-dodecanol binary eutectic phase change materials for low temperature solar thermal applications: Design, development and thermal analysis, Sol. Energy 155 (2017) 1373-1379. https://doi.org/10.1016/j.solener.2017.07.082.

[11] D. Li, T. Lenfant, V. Landry, D. Rodrigue, A. Kaboorani, X.A. Wang, Development and investigation of biobased binary eutectic phase change materials for low-temperature building applications: 1-Hexadecanol/1-Dodecanol and 1-Octadecanol/1-Dodecanol, J. Energy Storage 103 (2024) 114345. https://doi.org/10.1016/j.est.2024.114345.

[12] J. Shen, Z. Cai, C. Wang, X. Liu, R. Zheng, Preparation and thermal performances of 1, 10-decanediol-stearic acid eutectic as phase change material, Thermochim. Acta 690 (2020) 178648. https://doi.org/10.1016/j.tca.2020.178648.

[13] K. Fu, S. Mo, Q. Li, Z. Zhou, L. Jia, Y. Du, Y. Chen, Preparation and thermal performance of a novel 1,10-decanediol-paraffin/ expanded graphite composite phase change material for solar thermal utilization, Sol. Energy Mater. Sol. Cells 289 (2025) 113684. https://doi.org/10.1016/j.solmat.2025.113684.

[14] G. Ma, S. Liu, S. Xie, Y. Jing, Q. Zhang, J. Sun, Y. Jia, Binary eutectic mixtures of stearic acid-n-butyramide/n-octanamide as phase change materials for low temperature solar heat storage, Appl. Therm. Eng. 111 (2017) 1052-1059. https://doi.org/10.1016/j.applthermaleng.2016.10.004.

[15] R. Riaz, M. Ali, S. Yaqub, H. Nazir, A. Khan, K. Iqbal, W. Khalid, Z. Said, Bio-based eutectic PCM-enhanced clay bricks for passive thermal regulation in extreme heat conditions, J. Build. Eng. 123 (2026) 115815. https://doi.org/10.1016/j.jobe.2026.115815.

[16] Z.W. Ko, A. Wiguno, J. Joynson, M.J. Ashfold, I. Khoiroh, Enhancing passive cooling of photovoltaic modules using bio-based eutectic phase change materials and barium sulphate radiative cooling paint, Next Energy. 10 (2026) 100490. https://do

i.org/10.1016/j.nxener.2025.100490.

[17] Z. He, P. Yu, L. Niu, C. Zhang, C. Ma, Photovoltaic panel cooling with new co mposite of phase change materials and hierarchical nanoparticles, Energy 308 (202 4) 132910. https://doi.org/10.1016/j.energy.2024.132910.

[18] D. Sachan, J. Bhattacharya, Characterization of paraffin wax-based nano-enhanced phase change materials with Al_2O_3, CuO and Cu nanoparticles and their performan ce comparison for heat storage application, Therm. Sci. Eng. Prog. 66 (2025) 104 031. https://doi.org/10.1016/j.tsep.2025.104031.

[19] P. Liu, C. Wang, X. Cheng, S. Wang, Z. Wang, Preparation and photothermal inv estigation of PDA and CuNPs coupled modified expanded graphite with sodium ac etate trihydrate composite phase change materials, Sol. Energy 293 (2025) 113478. https://doi.org/10.1016/j.solener.2025.113478.

[20] K. Moulakhnif, Z. Moujoud, A.E. Majd, H.A. Ousaleh, A. Faik, S. Sair, A.E. Bo uari, Eutectic organic phase change materials integrated into inorganic geopolymer foam for low-temperature thermal energy storage in building applications, Process Saf. Environ. Protect. 202 (2025) 107750. https://doi.org/10.1016/j.psep.2025.107750.

[21] Y. Tan, P. Li, Y. Yao, H. Li, J. Zhong, J. Wu, Y. Zhang, J. Wang, Green prepara tion and performance research of n-octadecane@silica phase change microcapsules for building energy conservation, Constr. Build. Mater. 497 (2025) 143847. https:// doi.org/10.1016/j.conbuildmat.2025.143847.

[22] Z. Haddad, B. Buonomo, E. Abu-Nada, O. Manca, A comprehensive review on th e properties of micro/nano-encapsulated phase change materials: Single- to multi-la yered shells, Renew. Sust. Energ. Rev. 205 (2024) 114826. https://doi.org/10.1016/j. rser.2024.114826.

[23] S. Sharwan, P. Sikarwar, B. Mazumdar, Recent innovations in support materials fo r shape-stable organic composite phase change materials: A comprehensive review, Sol. Energy Mater. Sol. Cells 272 (2024) 112910. https://doi.org/10.1016/j.solmat.20 24.112910.

[24] Y. Ren, F. Jin, L. Yang, Q. Zhang, N. Zheng, C. Xu, Emerging porous supporting

materials for form-stable organic phase change materials, Sustain. Mater. Technol. 45 (2025) e01440. https://doi.org/10.1016/j.susmat.2025.e01440.

[25] Y. Liu, Y. Zhang, M. Li, Y. Wang, G. Li, Q. Yu, R. Tang, X. Yang, X. Li, Novel water-based composite phase change materials for cold energy storage applications, Renew. Energy 240 (2025) 122174. https://doi.org/10.1016/j.renene.2024.122174.

[26] K. Chopra, A.K. Pandey, A. Islam, R.K. Rajamony, M. Mansor, V.V. Tyagi, Enhancing charging/discharging performance of solar-assisted water heater integrated with stearic acid/expanded graphite as form-stable phase change material, J. Taiwan Inst. Chem. Eng. 178 (2026) 106406. https://doi.org/10.1016/j.jtice.2025.106406.

[27] J. Jacob, A.K. Pandey, N.A. Rahim, J. Selvaraj, J. Paul, Multi-wall carbon nanotubes tailored eutectic composites for solar energy harvesting, Energy 288 (2024) 129777. https://doi.org/10.1016/j.energy.2023.129777.

[28] X. Deng, C. Li, M. Yuan, H. Jiao, X. Sun, Y. Li, H. Yang, C. Wang, PDMS/graphene oxide coated wood-based composite phase change materials with efficient solar-thermal-electric conversion, Appl. Therm. Eng. 263 (2025) 125394. https://doi.org/10.1016/j.applthermaleng.2024.125394.

[29] B. Hu, J. Li, X. Du, Z. Zhang, H. Wang, $NH_4Al(SO_4)_2.12H_2O$-Na_2SO_4 eutectic-based phase change materials with excellent light absorbance, enhanced thermal conductivity, and high latent heat performance, J. Energy Storage 99 (2024) 113349. https://doi.org/10.1016/j.est.2024.113349.

[30] R. Wen, S. Zhu, M. Wu, W. Chen, Design and preparation of Ag modified expanded graphite based composite phase change materials with enhanced thermal conductivity and light-to-thermal properties, J. Energy Storage 41 (2021) 102936. https://doi.org/10.1016/j.est.2021.102936.

[31] Q. Zhang, Y. Chen, R. Liu, J. Luo, Efficiently all-weather anti-icing and de-icing coatings enabled by polyaniline microcapsules encapsulated phase change materials, Chem. Eng. J. 499 (2024) 156122. https://doi.org/10.1016/j.cej.2024.156122.

[32] J. Ning, J. Hu, M. Zhou, T. Wang, M. Chen, K. Wang, W. Wang, K. Jiang, In-situ pre-sodiation of Prussian blue for the construction of high-performance sodium-i

on batteries, Chem. Eng. J. 489 (2024) 151531. https://doi.org/10.1016/j.cej.2024.151531.

[33] F. Zhao, W. Yuan, H. Chen, H. Fu, Z. Li, J. Xiao, Y. Feng, Advances in Organic Porous Polymeric-Supported Photothermal Phase Change Materials, Carbon Energy 7 (2025) e719. https://doi.org/10.1002/cey2.719.

[34] H. Cheng, J. Guan, N. Yu, W. Xia, K. Zhang, H. Hu, Prussian Blue-Carbonized wood photothermal composites for efficient solar evaporation and seawater desalination, Sep. Purif. Technol. 357 (2025) 130230. https://doi.org/10.1016/j.seppur.2024.130230.

[35] C. Qiu, J. Zhou, X. Hu, M. Kang, X. Mu, Z. Zhang, Y. Long, Y. Zhu, J. Gao, G. Xu, L. Miao, Solar-driven interfacial evaporation coupling with photo-Fenton of floating Prussian blue/polypyrrole/paper film for volatile organic compounds-containing wastewater treatment, Sep. Purif. Technol. 362 (2025) 131735. https://doi.org/10.1016/j.seppur.2025.131735.

[36] P. Guo, X. Zhuo, K. Zhang, L. Zhang, D. Zhang, C. Wang, T. Nomura, R. Zhu, N. Sheng, C. Zhu, Z. Rao, Bioinspired flexible phase change composites for highly efficient solar-thermal-electric conversion and storage, Compos. Pt. B-Eng. 313 (2026) 113397. https://doi.org/10.1016/j.compositesb.2026.113397.

[37] A.N.B. Costa, J.L. Serra, I.D.L. Rodrigues, L.T.B. Mendonca, G. Pereira, E.M.S. Castanheira, S.F. Rodrigues, A.E.M. Paiva, S.R.S. Veloso, A.R.O. Rodrigues, G.S. Correia, Evaluation of the photothermal performance of the Prussian blue/hydroxyapatite composite, Mater. Today Commun. 46 (2025) 112598. https://doi.org/10.1016/j.mtcomm.2025.112598.

[38] S. Han, Y. Zheng, Y. Shang, J. Hu, S. Sun, J. Chen, L. Yang, Aliphatic polycarbonate-based photothermal elastomers: Tunable properties and degradability, J. Mater. Sci. Technol. 272 (2026) 161-170. https://doi.org/10.1016/j.jmst.2026.02.025.

[39] Y. Wang, Z. Liang, Z. Liang, W. Lv, M. Chen, Y. Zhao, Advancements of Prussian blue-based nanoplatforms in biomedical fields: Progress and perspectives, J. Control. Release 351 (2022) 752-778. https://doi.org/10.1016/j.jconrel.2022.10.007.

[40] M. Wieckowski, M. Krolikowski, M. Zywolko, L. Scheller, M. Dzida, Examination of eutectic phase change materials composed of diols and ionic liquids, J. Mol. Liq. 379 (2023) 121660. https://doi.org/10.1016/j.molliq.2023.121660.

[41] Z.K. Genc, C.A. Canbay, S.S. Acar, M. Sekerci, M. Genc, Preparation and thermal properties of heterogeneous composite phase change materials based on camphene-palmitic acid, J. Therm. Anal. Calorim. 120 (2015) 1679-1688. https://doi.org/10.1007/s10973-015-4478-3.

[42] K. Luo, D. Wu, Y. Wang, H. Fei, H. Jiang, Z. Ye, Preparation and characterization of lauric acid-stearic acid/fumed silica/expanded graphite thermally conductive enhanced composites, J. Energy Storage 73 (2023) 109151. https://doi.org/10.1016/j.est.2023.109151.

[43] Y. Chen, H. Zhang, C. Xu, R. Cong, G. Fang, Thermal properties of 1-hexadecanol/high density polyethylene/graphene nanoplates composites as form-stable heat storage materials, Sol. Energy Mater. Sol. Cells 237 (2022) 111580. https://doi.org/10.1016/j.solmat.2022.111580.

[44] B. Kalidasan, A.K. Pandey, R. Saidur, Y.N. Mishra, Z. Ma, V.V. Tyagi, Thermal performance and corrosion resistance analysis of inorganic eutectic phase change material with one dimensional carbon nanomaterial, J. Mol. Liq. 391 (2023) 123281. https://doi.org/10.1016/j.molliq.2023.123281.

[45] A.L.K. Bharathi, C. Manikandan, M. Bhuvanesh, S. Kalaiselvam, Experimental investigation on the thermal storage performance of nanocomposite-enhanced fatty acid eutectic PCM and the effect of ultrasonic vibration for application in cold storage, J. Energy Storage 101 (2024) 113797. https://doi.org/10.1016/j.est.2024.113797.

[46] M. Li, Z. Wu, H. Kao, Study on preparation and thermal properties of binary fatty acid/diatomite shape-stabilized phase change materials, Sol. Energy Mater. Sol. Cells 95 (2011) 2412-2416. https://doi.org/10.1016/j.solmat.2011.04.017.

[47] A. Sari, Eutectic mixtures of some fatty acids for low temperature solar heating applications: Thermal properties and thermal reliability, Appl. Therm. Eng. 25 (2005) 2100-2107. https://doi.org/10.1016/j.applthermaleng.2005.01.010.

[48] Z. Fan, Y. Zhao, X. Liu, Y. Shi, D. Jiang, Thermal properties and reliabilities of myristic acid-paraffin wax binary eutectic mixture as a phase change material for solar energy storage, Rsc Adv. 12 (2022) 12303-12309. https://doi.org/10.1039/D1RA09238C.

[49] R. Zhang, D. Chen, L. Chen, X. Cao, X. Li, Y. Qu, Preparation and thermal properties analysis of fatty acids/1-hexadecanol binary eutectic phase change materials reinforced with TiO_2 particles, J. Energy Storage 51 (2022) 104546. https://doi.org/10.1016/j.est.2022.104546.

[50] E.S. Goda, S. Lee, M. Sohail, K.R. Yoon, Prussian blue and its analogues as advanced supercapacitor electrodes, J. Energy Chem. 50 (2020) 206-229. https://doi.org/10.1016/j.jechem.2020.03.031.

[51] X. Wang, L. Cheng, Multifunctional Prussian blue-based nanomaterials: Preparation, modification, and theranostic applications, Coord. Chem. Rev. 419 (2020) 213393. https://doi.org/10.1016/j.ccr.2020.213393.

[52] J. Han, X. Meng, Q. Pang, F. Ma, Q. Li, An expanded graphite-based composite phase change material with 3D thermal conductive network prepared via mechanical exfoliation, Diam. Relat. Mat. 158 (2025) 112704. https://doi.org/10.1016/j.diamond.2025.112704.

[53] B. Wu, Y. Jiang, Y. Wang, C. Zhou, X. Zhang, J. Lei, Study on a PEG/epoxy shape-stabilized phase change material: Preparation, thermal properties and thermal storage performance, Int. J. Heat Mass Transf. 126 (2018) 1134-1142. https://doi.org/10.1016/j.ijheatmasstransfer.2018.05.153.

[54] M.A. Busquets, A. Novella-Xicoy, V. Guzman, J. Estelrich, Facile Synthesis of Novel Prussian Blue-Lipid Nanocomplexes, Molecules 24 (2019) 4137. https://doi.org/10.3390/molecules24224137.

[55] S. Hui, H. Zhang, G. Xu, J. Zhang, F. Xu, L. Sun, X. Lin, L. Ma, H. Peng, B. Li, E. Yan, H.J. Seifert, Bridge-grafted EG/BCN encapsulated PW with effectively improved thermal conductivity and battery thermal management performance, J. Energy Storage 104 (2024) 114661. https://doi.org/10.1016/j.est.2024.114661.

[56] Y. Dong, X. Yuan, High-efficiency electrothermal and electromagnetic interference shielding performance of expanded graphite/silicone film, Polym. Compos. 46 (2025) 506-514. https://doi.org/10.1002/pc.29002.

[57] Y. He, X. Wu, G. Hu, S. Wang, R. Feng, Highly flexible composite phase-change material PA-EG-AgNPs achieved through self-assembly of nano-silver for enhanced photothermal performance, J. Energy Storage 86 (2024) 111263. https://doi.org/10.1016/j.est.2024.111263.

[58] L. Geng, J. Wang, X. Yang, J. Jiang, R. Li, Y. Yan, J. Zhao, C. Liu, Synergistic enhancement of phase change materials through three-dimensional porous layered covalent triazine framework/expanded graphite composites for solar energy storage and beyond, Chem. Eng. J. 487 (2024) 150749. https://doi.org/10.1016/j.cej.2024.150749.

[59] J. Ren, T. Hu, W. Zhang, L. Li, W. Yuan, Enhanced photo-thermal conversion in phase change materials by Cu-Zn Bi-metallic metal-organic framework and expanded graphite, Sol. Energy Mater. Sol. Cells 281 (2025) 113326. https://doi.org/10.1016/j.solmat.2024.113326.

[60] T. Xiao, X. Shi, L. Gen, Y. Dai, J. Zhao, C. Liu, Synergistic enhancement of phase change materials through three-dimensional macropore lamellar structured MOF/EG composite for solar energy storage and beyond, Appl. Therm. Eng. 235 (2023) 121378. https://doi.org/10.1016/j.applthermaleng.2023.121378.

[61] Y. Huang, M. Zou, W. Chen, W. Luo, X. Hu, G. Zhu, S. Tan, X. Jiang, A Novel Room-Temperature Flexible Phase Change Material for Solar Energy Photothermal Conversion and Battery Thermal Management, ACS Sustain. Chem. Eng. 12 (2024) 4662-4675. https://doi.org/10.1021/acssuschemeng.3c08489.

[62] J. Shen, W. Dong, X. Xu, Z. Gong, B. Ye, X. Wang, F. Zhou, Performances of eutectic phase change composites containing CNTs/GO/PVA oriented aerogels coated with EP/CNTs/CFR for Li-ion batteries thermal management in wide temperature range, Energy 339 (2025) 139095. https://doi.org/10.1016/j.energy.2025.139095.

[63] H. Su, P. Lin, D. Li, Y. Chen, Reduced Graphene Oxide/Cellulose Sodium Aeroge

l-Supported Eutectic Phase Change Material Gel Demonstrating Superior Energy Conversion and Storage Capacity toward High-Performance Personal Thermal Management, ACS Appl. Mater. Interfaces 16 (2024) 3334-3347. https://doi.org/10.1021/acsami.3c15470.

[64] C. Li, M. Wang, B. Xie, Y. He, Carbon-decorated diatomite stabilized lauric acid-stearic acid as composite phase change materials for photo-to-thermal conversion and storage, Renew. Energy 229 (2024) 120731. https://doi.org/10.1016/j.renene.2024.120731.